



Originally published as:

Dahm, T., Hainzl, S., Fischer, T. (2010): Bidirectional and unidirectional fracture growth during hydrofracturing: Role of driving stress gradients. - Journal of Geophysical Research, 115, B12322

DOI: 10.1029/2009JB006817

Bidirectional and unidirectional fracture growth during hydrofracturing: Role of driving stress gradients

Torsten Dahm,¹ Sebastian Hainzl,² and Tomas Fischer³

Received 24 July 2009; revised 19 July 2010; accepted 19 August 2010; published 23 December 2010.

[1] An unexpected observation from induced seismicity during stimulation experiments was the identification of asymmetric bidirectional and unidirectional growth of the seismic front and back front, indicating asymmetric growth of the hydrofracture itself. We develop and analyze a new analytical hydrofracture model that considers for the first time the effect of stress and pore pressure gradients on growth. It is based on plane strain linear elastic fracture mechanics and further considers 1-D laminar flow, the opening shape of the fracture, and a Griffith fracture criterion. The model explains asymmetric bidirectional growth during the injection and bidirectional and unidirectional growth during the postinjection phase. Analytical relations are derived for both cases to estimate the front and back front of the seismicity as a function of injection pressure, volume rate, stress gradients, viscosity, and elastic modules of the rock. Interestingly, the postinjection phase can be described by self-similar solutions, which depend only on the stress gradient and the injection pressure and which predict a parameter-independent length increase of the fracture after the injection stops. We use the theoretical opening shape of the fracture to calculate time- and space-dependent Coulomb stress changes in the rock in order to predict the patterns of induced seismicity in the neighborhood of the fracture. The model explains in detail the patterns of earthquakes induced during hydrofracturing stimulation experiments in a low-permeable gas field sandstone in west Texas, and we estimate a lateral stress or pore pressure gradient of more than 0.8 MPa km^{-1} . If the downhole net pressure during the experiments was 1 MPa, the gradient is constrained at about 10 MPa km^{-1} .

Citation: Dahm, T., S. Hainzl, and T. Fischer (2010), Bidirectional and unidirectional fracture growth during hydrofracturing: Role of driving stress gradients, *J. Geophys. Res.*, 115, B12322, doi:10.1029/2009JB006817.

1. Introduction

[2] Hydraulic fracturing is performed in borehole wells within sections sealed off from the fluid pressure above and below. Fluid is injected at a constant flow rate. During injection the wellbore inside the sealed section is pressurized for several minutes until the initiation of the tensile fracture, which is usually recognized by a breakdown of the pressure. After initial breakdown, injection continues until the pressure is stabilized. Injection is then stopped, and pressure is allowed to decay. The in situ principal stress magnitudes within the rock are estimated from the fracture initiation pressure, the shut-in pressure at which the fluid flows into the newly formed fracture, the pore pressure of the formation after the shut-in phase, and the fracture reopening pressure during a second cycle of hydrofracturing [e.g., Pollard and Fletcher, 2005; Economides and Nolte, 2003,

chapter 3]. The orientation of the least horizontal stress can additionally be estimated by mapping well breakouts [e.g., Pollard and Fletcher, 2005]. Well stimulation, i.e., hydraulic fracturing experiments lasting longer and realizing larger injection volumes, have further been used for hot dry rock geothermal energy to create artificial cracks (heat exchanger) in the surrounding material of the heat production well. The system of artificially formed cracks increases the effective permeability and the heat exchanging surface of the rock and thus the productivity of the power plant. Well stimulation is also applied to hydrocarbon reservoirs to enhance the productivity of fluid extraction. For stimulation experiments it is important to predict and measure the length and width of the newly formed fractures.

[3] Monitoring and locating acoustic emissions and microseismic clouds accompanying stimulation experiments is a novel technique to characterize the newly formed fracture system and other physical properties of the formation [Cornet and Julien, 1989; Cornet and Yin, 1995; Rutledge and Phillips, 2003; Shapiro et al., 1997]. The hypocenter can nowadays be located within $\pm 20 \text{ m}$ if borehole sensor arrays are used [e.g., Eisenblätter, 1988; House, 1987; Dahm et al., 1999; Manthei et al., 2003; Moriya et al., 2006; Rutledge et al., 2004; Oye et al., 2004; Evans et al., 2005; Eisner

¹Institut für Geophysik, Universität Hamburg, Hamburg, Germany.

²GFZ German Research Centre for Geosciences, Potsdam, Germany.

³Faculty of Science, Charles University in Prague, Prague, Czech Republic.

where the formation permeability is small or the injection pressure is large. One such stimulation experiment was conducted in a gas field in Texas, where the induced seismic cloud indicated 1-D growth of the fracture [e.g., *Eisner et al.*, 2006; *Fischer et al.*, 2009]. We find very good agreement and discuss this application in section 3 before we conclude our main findings in section 4.

2. Fracturing Model

[9] We assume a homogeneous isotropic porous rock mass embedding the newly formed fracture. The fracture is growing in $\pm x$ direction and opens in y direction (Figure 1). The opening is Δu , and the average half opening is defined by h . The general notation is summarized in the notation section. The fracture is idealized by a 2-D crack (plane strain problem), which is valid if the crack extension in z direction is much longer than in x direction or if growth in z direction is limited by sealing layers on which slip occurs (compare KGD model). The approximation may also hold in the central plane of symmetry of an ellipsoidal fracture.

[10] The injection of fluids is restricted to a single fixed line or plane in space from which the fracture begins to grow and the fracture is assumed to be completely sealed along its surface. The opening shape and size of the fracture are controlled by the internal effective driving pressure P , by the length $2a$ of the fracture and by the fracture toughness of the rock, K_c . During injection, the driving pressure P in the fracture is expressed as the sum of the net overpressure (net pressure), P_{net} , and the possible fluid-related pressure drop within the wings of the newly formed fracture. At the injection point $x = 0$ we have $P(0, t) = P_{\text{net}}(0, t) = P_0(t)$. The net pressure is the difference between the internal downhole pressure, P_d , and the external normal stress (compression) acting on the outer fracture wall. The external stress is controlled by both the tectonic normal stress, σ_{yy} , and the pore pressure of the formation, P_p . Within a porous rock formation with Biot's constant α , the internal net pressure is therefore defined by $P_{\text{net}} = P_d - (\sigma_{yy} - \alpha P_p)$, where we assume that the exact effective stress law [Nur and Byerlee, 1971] is valid [see, e.g., *Zoback*, 2007]. The equation is similar to equations 5-3 and 5-4 of *Economides and Nolte* [2003], except that the effective stress instead of the total stress is used. Note that the three influences, tectonic stress, pore pressure, and internal pressure, sum up in a single net pressure and cannot be individually resolved.

[11] Our model considers stress and pressure gradients in the direction of fracture growth (x direction). We assume linear pressure and stress changes only, i.e., constant gradients, and define g , g^v , and g^{eff} as the gradients of the net pressure, viscous pressure drop, and effective driving pressure, respectively, where $g^{\text{eff}} = g + g^v$. A nonzero gradient $g \neq 0$ may stem (1) from the gravity effect within the injection fluid if the fracture is extended in vertical direction (P_d is changing), (2) from a nonzero pore pressure gradient (P_p is changing), or (3) alternatively from a nonzero tectonic stress gradient (σ_{yy} is changing). We assume that the net pressure gradient is pointing in growth direction x . Then the tectonic stress gradient or the pore pressure gradient are both pointing in $-x$ direction (Figure 1).

[12] The injection experiment consists in general of four subsequent possible phases: (1) the injection phase with

bidirectional fracture growth, (2) the postinjection phase with bidirectional growth, (3) a possible postinjection phase with unidirectional growth, and (4) a possible after-injection phase with a slow wholesale movement of the fluid-filled fracture.

[13] The injection phase 1 (see Figure 1) is characterized by a point-like massive injection of fluids at $x = 0$ lasting several minutes or tens of minutes and, after initiation, is usually performed under nearly constant injection downhole pressure and volume rate. The injection downhole pressure has a larger magnitude than the least tectonic stress plus the formation pore pressure, so that a positive net and driving pressure exists and a hydrofracture is created and driven in $+x$ and $-x$ direction (bidirectional growth). The position and the velocity of the crack tips of the short and long wings are denoted by a_s , a_l and v_s , v_l , respectively, and the bidirectional growth is symmetric if $|v_s(t)| = |v_l(t)|$, where t is the time. Otherwise, it is asymmetric; that is, one wing of the fracture is growing faster than the other. Asymmetric growth with a longer wing in $+x$ direction occurs if $g > 0$.

[14] The postinjection phase 2 starts immediately after stopping the injection. For a short time period, the hydrofracture continues to grow bidirectional until the ambient net pressure within the fracture is reduced below a critical value that is necessary to further drive the fracture. According to the Griffith criterion, the stress intensity factor at both of the fracture tips, $K^+(t)$ or $K^-(t)$, is equal to K_c . If $g = 0$, the problem is symmetric and $K^+ = K^-$ so that the postinjection phase 2 stops simultaneously at both ends.

[15] If $g > 0$, however, a third phase (phase 3) may follow this postinjection phase, in which the tip at the shorter wing is not moving and the longer wing continues to grow until the stress intensity factor K^+ has also decreased to the critical value K_c . The fracture growth becomes unidirectional during this phase (see phase 3 in Figure 1b).

[16] If $g > 0$ and if enough fluid has been injected, the fracture may have grown to an overcritical length, $2a \geq 2a_c$. Then, driven by the apparent "buoyancy force" at the tip of the longer wing, the problem is characterized by a slow wholesale movement in a direction of positive net pressure gradient g (phase 4). Phase 4 is usually very slow and difficult to observe for hydrofracturing experiments. It has, however, often been observed in the context of magma movement beneath volcanoes [e.g., *Dahm*, 2000b, 2000a, and references therein].

[17] The theoretical description of fracture growth should possibly involve processes such as the elastic rock emplacement under varying driving pressure, the viscous flow problem under moving boundaries, and the rock fracturing problem at the crack tip under a slowly changing shape of the fracture. The fracture growing velocity is observed to be small compared to a wave velocity, so that inertia terms can be neglected. The three processes are coupled by the driving stress. Complete analytical solutions to such a problem are difficult and not known to us, and usually, simplifying assumptions are introduced. In our study, for instance, we neglect the details of the shape of the fracture when estimating the viscosity-controlled pressure drop from flow. Laminar flow is assumed and characterized by a constant viscous pressure gradient and effective channel thickness. In combination with the constant net pressure

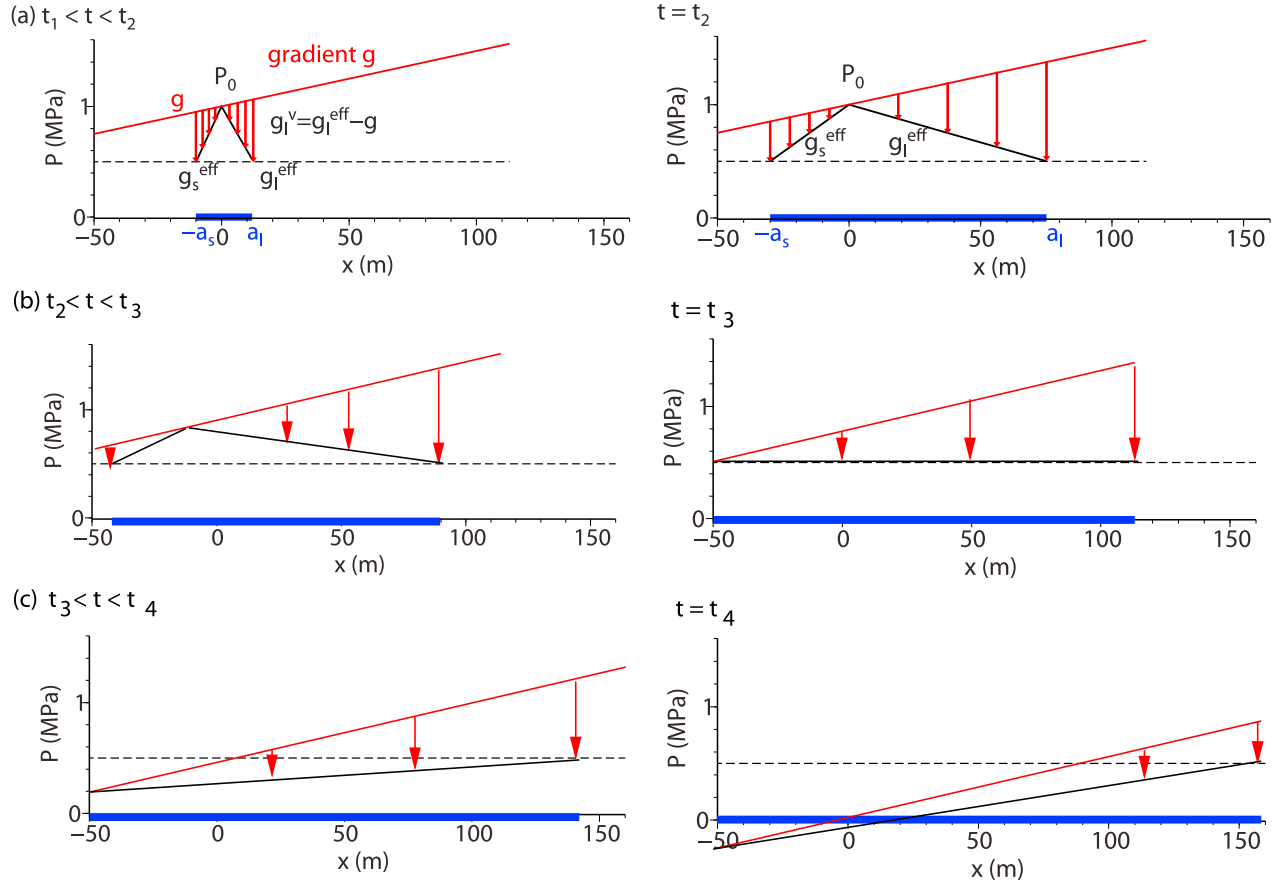


Figure 2. Sketch of the effective net pressure (black line) and the driving stress (no-flow net pressure, red line) for increasing growing length of the asymmetric fracture (indicated by the thick blue line). (a) The injection phase, (b) the postinjection phase with bidirectional growth and (c) the postinjection phase with unidirectional growth. The injection driving pressure P_0 and the injection point are indicated. The red arrows indicate the pressure drop that is accomplished by viscous fluid flow. For simplicity, we indicate a constant critical effective net pressure at the tips of the fracture (dashed line). In theory, the tip net pressure is slightly decreasing with increasing fracture length.

gradient we employ cracks under time-dependent, spatially constant driving pressure gradients and consider the stress intensity factor K^\pm at both crack tips. As we show below, the fracture criterion at the crack tip is essential in our model to the understanding of the postinjection phase 2 and the unidirectional growing self-expanding crack in phase 3.

2.1. Elementary Crack Solutions and Concept

[18] Appendix A gives the fracture opening and stress intensity factors K^\pm for opening mode cracks under different driving pressure and positions of the injection point. In the most general case, K^\pm depends on the fracture half-length a , the position a' (injection point or point of zero flow), the maximal internal driving pressure P_0 , and the effective gradients g_s^{eff} and g_l^{eff} in the shorter and longer wing of the fracture (see equations (A14) and (A15)). Since the Griffith fracture criterion is fulfilled during growth, we always have $K^\pm = K_c$. The internal driving pressure at both tips, however, may slightly differ if the shape of the tip differs (see (A14) and (A15)).

[19] Fluid flow is assumed in two opposite directions away from the injection point. As long as the fracture is growing, the net pressure (no-flow) is larger than the effective driving pressure at the tips. The pressure drop from the high net driving pressure to the relatively small tip driving pressure is accomplished by viscous flow.

[20] Figure 2 sketches how the effective driving pressure changes with fracture length during the three phases (1–3). During injection, the injection point and net pressure $P_{\text{net}}(x=0) = P_0$ is held constant. During phase 1 the high net pressure at the tip of both wings is reduced by viscous pressure drag from flow in opposite directions. During phase 2 the injection has stopped, the ambient net and driving pressure decreases as a result of volume decompression, and the point of zero flow slowly moves backward in the $-x$ direction. At the end of phase 2 the net pressure at the tip of the shorter wing is equal to the driving pressure necessary to just start or stop fracture growth there. The effective driving pressure is then constant over the whole length of the fracture, and the fracture opening is elliptical (see Figure A1, top). During the postinjection phase 3 the fluid flow and fracture growth is

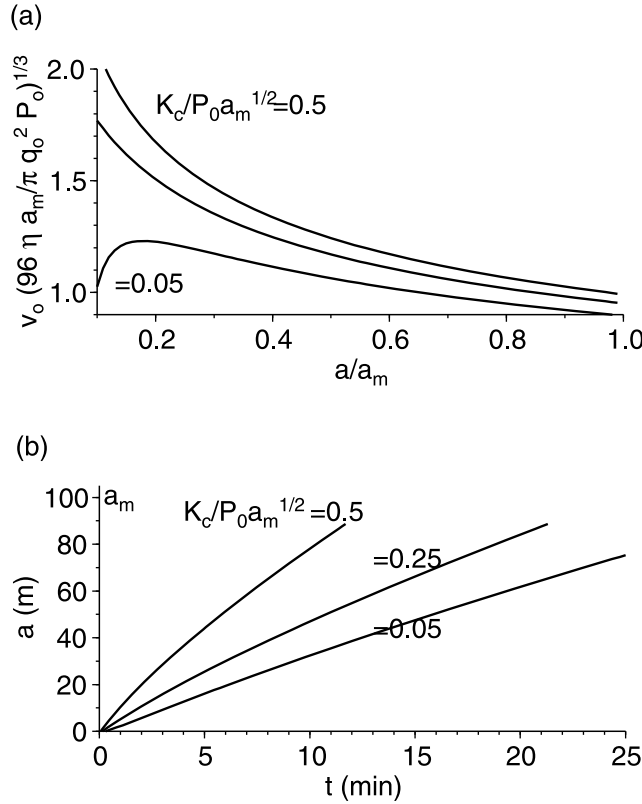


Figure 3. (a) Normalized crack tip velocity $v_0 (96 \eta a_m / \pi q_0^2 P_0)^{1/3}$ (see equation (6)) as a function of normalized length a/a_m (a_m is the length at the end of the injection phase 1 against different parameters of relative overpressure $K_c/P_0 \sqrt{a_m}$). (b) Solution was integrated to time-dependent fracture length, where absolute values are plotted. The examples uses $a_m = 100$ m, $q_0 = 7 \times 10^{-3}$ m² s⁻¹, $K_c = 5$ MPa \sqrt{m} , and $\eta = 150$ Pa. P_0 was varied at 1, 2, and 10 MPa.

unidirectional in $+x$. With increasing fracture length, the net pressure at the tip of the shorter wing is further decreasing below its critical value, and the opening shape of the fracture more and more resembles a teardrop-shaped crack (Weertman crack, see Figure A1, middle). Phase 3 is completed when the effective driving pressure at the tip of the shorter wing is negative and 1/3 of the driving pressure at the longer wing's tip [e.g., Dahm, 2000b].

[21] The viscous pressure gradient is equated by $g^v = g^{\text{eff}} - g$. Figure 2 shows that $|g^v|$ becomes smaller the longer the fracture is growing. This indicates that the flow velocity may decrease with increasing fracture length. However, the average thickness during the injection phase will increase with length, which has an opposite effect on flow velocity.

[22] The principle to derive the crack tip velocity in both fracture wings is similar for all three phases. We use the boundary conditions for g^v as discussed with Figure 2. We further equate the average half opening of the fracture, h_s and h_l , as a function of fracture wing length a_s and a_l , and apply a "laminar flow law" as

$$v = -C h^2 g^v \sim h^2 g^v. \quad (1)$$

C is a constant depending on the dynamic viscosity of the fluid and possibly other elastic parameter. Both h and g^v are functions of a , P_0 , K_c , and a' (see Appendix A). Equation (1) depends explicitly on the length of the fracture but only implicitly on time. We assume that during injection, equation (1) can be applied to derive the length-dependent velocities v_s and v_l in both wings of the fracture and take further advantage of the length-dependent description below. The time-dependent velocity of the fracture tips, however, can be derived from $v = v(a)$ by direct integration,

$$dt = v^{-1}(a) da \quad \text{and thus} \quad t(a_s) = \int_0^{a_s} v_s^{-1}(a) da$$

$$\text{and} \quad t(a_l) = \int_0^{a_l} v_l^{-1}(a) da. \quad (2)$$

2.2. Injection Phase 1 Under Driving Stress Gradients

[23] The stress intensity factor at the tip is equal to K_c . Using (A13), the effective pressure gradient is given by (see Figure A3)

$$g^{\text{eff}}(a) = g_s^{\text{eff}}(a) = \frac{\pi}{2a} \left(P_0 - \frac{K_c}{\sqrt{\pi a}} \right) \quad \text{and} \\ g_l^{\text{eff}}(a) = -g_s^{\text{eff}}(a), \quad (3)$$

where a (positive quantity) is the distance of the tip 1 or 2 to the injection point. The viscous pressure drop in both wings is equated by

$$g_s^v = g_s^{\text{eff}} - g > 0 \quad \text{and} \quad |g_l^v| = |g_l^{\text{eff}}| + g, \quad g_l^v < 0. \quad (4)$$

If $g = 0$ (bidirectional symmetric growth), the given equations are sufficient to derive v . From the balance of influx volume rate q_0 ,

$$\frac{q_0(t)}{2} = q_s(t) = q_l(t) = +2h_l(t)v_l(t) = -2h_s(t)v_s(t),$$

and using $a(t) = a_s(t) = a_l(t)$ one finds a length-dependent formulation as

$$\frac{q_0(a)}{2} = q_s(a) = q_l(a) = +h_l(a)v_l(a) = -h_s(a)v_s(a). \quad (5)$$

From (1), (4), and (5) this leads to

$$v_0 = -v_s = +v_l = \left[\frac{1}{48\eta} q_0^2 g^{\text{eff}} \right]^{1/3} \\ = \left[\frac{\pi}{96\eta} \frac{q_0^2}{a} \left(P_0 - \frac{K_c}{\sqrt{\pi a}} \right) \right]^{1/3}, \quad 0 \leq a \leq a_m; \quad (6)$$

a_m is the half-length of the "symmetric fracture" at the end of the injection phase, and v_0 is the length-dependent growth velocity if driving stress gradients are zero, i.e., $g = 0$ (bidirectional, symmetric growth). Usually, both P_0 and q_0 are estimated during injection and vary only smoothly with time or length of the fracture. Then, velocity scales approximately with $v_0 \sim a^{-1/3}$. A slight dependency on $K_c/P_0 \sqrt{a_m}$ is observed if the net pressure at $x = 0$ and P_0 is

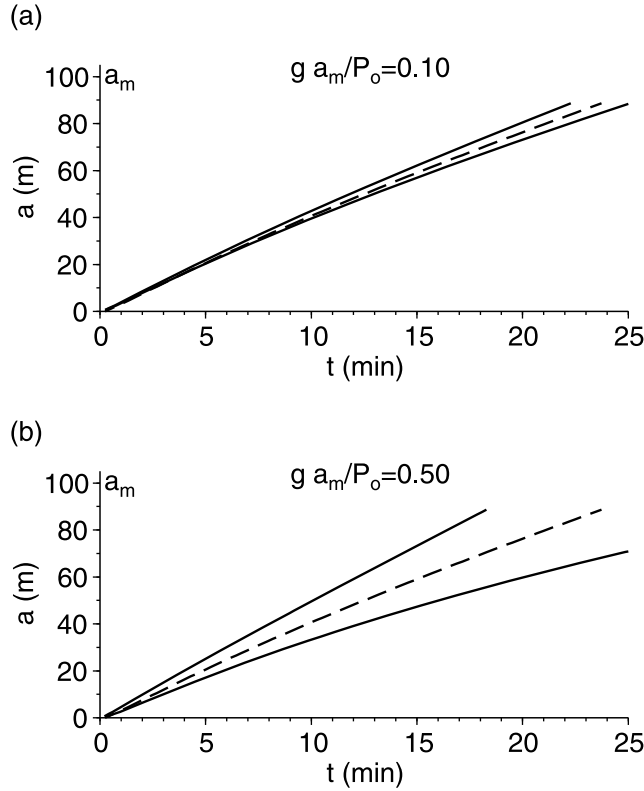


Figure 4. Asymmetric time-dependent crack length a_1 and a_2 . The dashed line indicates the symmetric wing length for $g = 0$. The continuous lines for (a) $g = 1 \text{ MPa km}^{-1}$ and (b) $g = 5 \text{ MPa km}^{-1}$. The following parameters have been used: $K_c = 5 \text{ MPa } \sqrt{\text{m}}$, $P_0 = 1 \text{ MPa}$, $a_m = 100 \text{ m}$, $q_0 = 10^{-2} \text{ m}^2 \text{ s}^{-1}$, and $\eta = 150 \text{ Pa s}$.

small (Figure 3). The length $a(t)$ is obtained by numerical integration of $v = da/dt$ and leads to a function approximately as $a \sim t^{3/4}$. A larger net pressure is leading to a faster growth than a smaller one. However, although the absolute values of $a(t)$ differ for different ratios $K_c/P_0\sqrt{a_m}$ (Figure 3), the shape of the different curves is similar, and it is thus not very likely that this ratio can be resolved against changes of the fluid viscosity, which also controls the absolute velocity of growth.

[24] The injection phase is mainly flow rate controlled. Observing a symmetric bidirectional growth and measuring q_0 and $a(t)$ (and thus $v = da/dt$) gives the possibility to estimate the “effective thickness” of the fracture, $h^{\text{eff}} = q_0/(2v)$, and to compare this with the elastic average thickness $h = [(1 - \nu)/4\mu]\pi a P_0$ (see (A12) for $g = 0$; P_0 has to be measured).

[25] What does change when $g > 0$? Equation (1) can now be written as

$$v_s = -v_0(a) \left(1 - \frac{g}{g^{\text{eff}}(a)}\right) \text{ and } v_l = v_0(a) \left(1 + \frac{g}{g^{\text{eff}}(a)}\right) \quad \text{with } v_0(a) = \frac{1}{3\eta} h(a)^2 g^{\text{eff}}(a). \quad (7)$$

Since $g^{\text{eff}}(a)$ and $h(a)$ are both independent of g (see also Figure 2), velocity change in both wings is only controlled by the changing viscous gradient (see equation (7)). The

time-dependent solution can be discussed by numerical integration of (2) to derive the time-dependent length and the time-dependent growth velocities of both wings (Figure 4). The variable a_m , the half-length of the “symmetric fracture” at the end of the injection phase, is introduced as normalization factor. If $g a_m$ is small compared to the injection driving pressure P_0 (net pressure at $x = 0$), the asymmetric growth is small and the growth velocity of both wings decreases with time. However, if $g a_m$ is of similar size as P_0 , the effect is significant. The longer wing grows faster and at nearly constant rate, while the shorter wing velocity slows down quickly.

[26] The numerical integration illustrated in Figure 4 confirms the derivation given by Fischer *et al.* [2009], e.g.,

$$\frac{1}{2}(a_s(t) + a_l(t)) \approx a(t) \quad \text{and} \quad \pi \left(\frac{a_l(t) - a_s(t)}{a_s^2(t) + a_l^2(t)} \right) \approx \frac{g}{P_0}. \quad (8)$$

Note that the different factor of $\pi/2$ between the results of Fischer *et al.* [2009] and (8) results from the fracture mechanical approach used here. Relation (8) can be used to estimate the driving stress gradient g directly from the time-dependent lengths of both fracture wings.

2.3. Bidirectional Growth in the Postinjection Phase 2

[27] The bidirectional growth in the postinjection phase 2 is maintained by the remaining driving pressure in the fracture at the end of the injection phase. The mechanism is qualitatively described in Figure 2. The fracture is now viewed as “finite volume crack,” and the internal overpressure decreases with fracture growth (decompression effect), resulting in a slowing down of growth. At the beginning time t_m of the postinjection phase the fracture has the length $2a_m$, a driving pressure at $x = 0$ of $P_{0m} = P_0(t_m)$ and an internal volume (cross-sectional area) of A_m (calculated from the average thickness h in (A12) times length). We first discuss the case when $g = 0$. Introducing a normalized volume as $A'_m = A_m/f a_m^2$, $f = [4(1 - \nu)\pi]/3\mu$, a normalized fracture toughness as $K'_{cm} = K_c/\sqrt{\pi a_m}$ and a relative length as $a' = a/a_m$, the driving stress at $x = 0$ and for $a > a_m$ ($a' > 1$) is (see (A12))

$$P_0(a') = \frac{A'_m}{(a')^2} - 2K'_{cm} \frac{1}{\sqrt{a'}}, \quad (9)$$

and the effective pressure gradient is calculated from (A12) as

$$a_m g^{\text{eff}}(a') = \frac{\pi}{2a'} \left(P_0(a') - K'_{cm} \frac{1}{\sqrt{a'}} \right). \quad (10)$$

Setting $g^{\text{eff}}(a') = 0$, the maximal postinjection length $a_{b\text{max}}$ is calculated as

$$a_{b\text{max}} = a_m \left(\frac{P_{0m}}{3K'_{cm}} + \frac{2}{3} \right)^{2/3}. \quad (11)$$

For instance, if the half-length of the fracture at the end of the injection phase was $a_m = 64 \text{ m}$, the downhole injection net pressure $P_{0m} = 1 \text{ MPa}$ and the fracture toughness is $K_c = 10 \text{ MPa } \sqrt{\text{m}}$, the postinjection half-length is $a_{b\text{max}} \approx 1.1 a_m \approx 70 \text{ m}$. The postinjection length increases when the ratio

between injection pressure and fracture toughness is larger, and vice versa, measuring the relative postinjection length from induced seismicity may be used to estimate the fracture toughness in the formation.

[28] What happens if $g \geq 0$? Phase 2 is then associated with a reorganization of internal flow, such that the point of zero flow is moving toward the tip at the shorter wing 1. This is plausible because the viscous pressure gradient is $|g_s^v(t)| < |g_t^v(t)|$. The analytical derivation is possibly difficult. However, at the end of the postinjection phase 2 and for $g \geq 0$ the point of zero flow is at the tip of the shorter wing at a_s . The flow-related viscous pressure gradient at the end of phase 2 is just compensating the gradient of the driving stress, and $g^v = -g$. Then g^{eff} is zero, and the postinjection phase enters a different mode which we defined as phase 3 (Figure 2). Therefore, at the end of phase 2 and beginning of phase 3 the growth velocity at the tip of the longer wing is well defined and may be used to estimate g .

2.4. Unidirectional Growth in the Postinjection Phase 3

[29] The postinjection phase 3 takes place only if $g > 0$. It starts at time t_3 when the fracture has a half-length of $a_3 = a(t_3)$. The opening shape of the fracture at time t_3 is elliptical and symmetric, since $g^{\text{eff}}(t_3) \approx 0$ (see Figure A1, top). We now define $x = 0$ at the tip at the shorter wing of the fracture (thinner tip), which remains fixed during unidirectional growth (see Figure 1). The tip at the longer wing (thicker tip) is at a distance $2a(t)$ from $x = 0$ and grows with velocity $v(t)$ in $+x$ direction. Similar to before, we define the time-dependent effective driving pressure by $P(t) = P_0(t) + g^{\text{eff}}x(t)$, noting that $P_0(t)$ is now the ambient overpressure at the midpoint of the fracture. The midpoint of the fracture is moving with velocity $v(t)/2 = da(t)/dt$.

[30] The problem simplifies if a midpoint-fixed, moving coordinate system ("primed") is introduced, $x = x' + a(t)$ and $y' = y$ (see Figure 1, phase 3). In the absolute system, the position of the midpoint of the fracture is $x_{\text{mid}} = a(t)$, and at the tip of the longer wing $x_{\text{tip}} = 2a(t)$. The postinjection phase lasts from $t_3 \leq t \leq t_4$, and the duration is associated with a continuously increasing half-length $a(t)$ from $a(t_3) = a_3 \leq a(t) \leq a_4 = a(t_4)$. The growing velocities at time t_3 and t_4 are defined by $v_3 = v(t_3)$ and $v_4 = v(t_4)$, respectively. Equivalently, overpressure, fracture volume, and average thickness at times t_3 and t_4 are declared by indices 3 and 4. The driving pressure $P_0(t)$ is the largest at the time t_3 and then continuously decreases, while $g^{\text{eff}}(t)$ is zero at time t_3 and then continuously increases with time. All equations in the moving coordinate system may be expressed as a function of $a = a(t)$. Since a can be directly measured from seismicity, the length-dependent approach already allows one to estimate key parameter of the problem. In a final step, however, we introduce the time dependency of the solution.

[31] Equation (A2) is rewritten in the primed system as

$$\Delta u(x', a) = \frac{(1-\nu)}{\mu} (2P_0(a) + g^{\text{eff}}(a)x') \sqrt{a^2 - (x')^2}, \quad (12)$$

where $-a \leq x' \leq a$ and $P_0(a)$ is the driving pressure at $x' = 0$. $P_0(a_3)$ is accordingly the driving pressure at $x' = 0$ when the

fracture has grown to the half-length a_3 . The static pressure gradient in (A2), g , is replaced by the length-dependent effective driving pressure gradient $g^{\text{eff}}(a) = g - |g^v(a)|$, where g^v is the average viscous pressure gradient along the fracture caused by unidirectional fluid movement inside the crack in $+x$ direction.

[32] The stress intensity factor at the tip of the longer wing is constant and equal to the fracture toughness,

$$K_c = K^+ = \sqrt{\pi a} \left(P_0(a) + \frac{g^{\text{eff}}(a)}{2} a \right) \quad \text{or} \quad P_0(a) = \frac{K_c}{\sqrt{\pi a}} - \frac{g^{\text{eff}}(a)}{2} a. \quad (13)$$

The stress intensity factor at the tip of the shorter wing is equal to the fracture toughness at time t_3 but decreases continuously after the longer wing begins to grow. This,

$$K_c = K^-(t_3) = \sqrt{\pi a_3} \left(P_0(a_3) - \frac{g^{\text{eff}}(a_3)}{2} a_3 \right),$$

combined with (13) leads to

$$P_0(a_3) = \frac{K_c}{\sqrt{\pi a_3}}, \quad \text{and} \quad g^{\text{eff}}(a_3) = |\epsilon| \approx 0, \quad (14)$$

where ϵ is arbitrarily small. The effective driving pressure is thus constant at the beginning of the postinjection phase, and the fracture opening shape is elliptical and symmetric. For $a > a_3$ ($t > t_3$) the driving stress is linear with x' , and the type of fracture opening belongs to the family of so-called Weertman cracks.

[33] For $t > t_3$ we find $K^-(t) > 0 < K_c$, and the transition from a symmetric elliptical crack to a fracture with teardrop shape at time t_4 is reached when $K^- = 0$, since then the ambient pressure cannot be further decreased without a beginning closure at the tip of the shorter wing [e.g., Dahm, 2000b].

[34] The cross-sectional area is expressed by (see (A3))

$$A(a_3) = A_3 = \frac{(1-\nu)}{\mu} \pi a_3^2 P_0(a_3) = \frac{(1-\nu)}{\mu} \pi a_3^2 \left(\frac{K_c}{\sqrt{\pi a_3}} \right). \quad (15)$$

The bulk modulus of the fluid is assumed to be large, so that the fluid volume, or cross-sectional area, is approximately constant, i.e., $A(a) \approx A_3$:

$$A_3 = \frac{(1-\nu)}{\mu} \pi a^2 \left(\frac{K_c}{\sqrt{\pi a}} - \frac{g^{\text{eff}}(a)}{2} a \right). \quad (16)$$

As a result of the expansion of the fracture the ambient overpressure at $x' = 0$ decreases with

$$P_0(a) = \frac{K_c}{\sqrt{\pi a_3}} \left(\frac{a_3}{a} \right)^2 = P_0(a_3) \left(\frac{a_3}{a} \right)^2. \quad (17)$$

From (15) and (16) we find

$$\begin{aligned} g^{\text{eff}} &= \frac{2}{a} \left(\frac{K_c}{\sqrt{\pi a}} - \frac{a_3^2}{a^2} \frac{K_c}{\sqrt{\pi a_3}} \right) = \frac{2K_c}{a\sqrt{\pi a}} \left(1 - \left(\frac{a_3}{a} \right)^{3/2} \right) \\ &= \frac{2P_0(a_3)}{a_3} \left[\left(\frac{a_3}{a} \right)^{3/2} - \left(\frac{a_3}{a} \right)^3 \right]. \end{aligned} \quad (18)$$

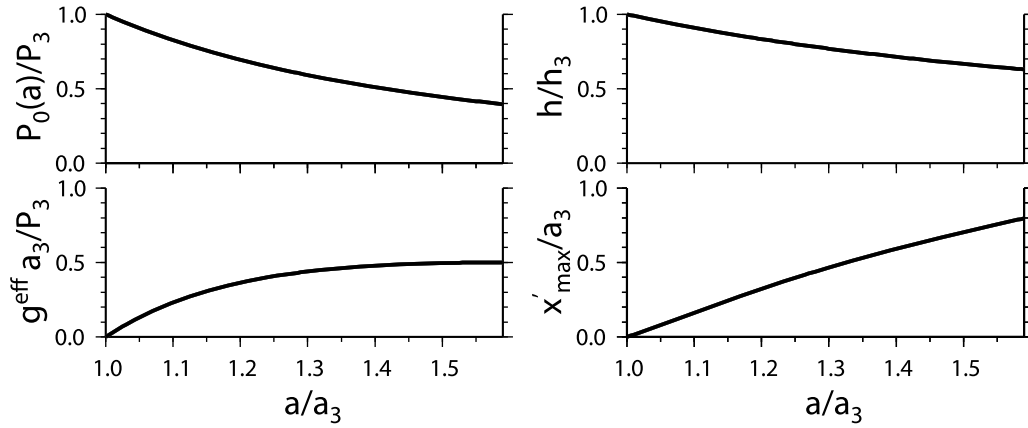


Figure 5. (left) Net pressure P_0 and the effective pressure gradient g^{eff} and (right) the average fracture half thickness h and the position of maximal opening x'_{max} are plotted as a function of fracture half-length a . Parameters are $K_c = 10$ MPa, $a_3 = 100$ m, $\mu = 30$ GPa, $\nu = 0.25$, $\eta = 10^4$ Pa s. The curves are all independent of g .

The driving pressure gradient is zero for $a \rightarrow a_3$. It has a maximum at $dg^{\text{eff}}/da = 0$, i.e., at $a = a_4 = 2^{2/3}a_3$, which is $g^{\text{eff}}(a_4) = \frac{1}{2}P_0(a_3)/a_3$. Using the nonpenetrating condition, $P_0(a) \geq (g^{\text{eff}}/2)a$, together with (13) and (18), the maximal length of the fracture is equated to $a = 2^{2/3}a_3 \approx 1.59a_3$, i.e., exactly to the length where the pressure gradient has its maximum. It is noteworthy that the maximal length of the self-expanding, unidirectional growing fracture in phase 3 is independent of the elastic parameter, ambient driving pressure, or other initial conditions.

[35] With (16) and (18) we find for the average half thickness of the fracture

$$h(a) = \frac{A_3}{4a} = \frac{(1-\nu)}{4\mu} K_c \sqrt{\pi a} \left(1 - \frac{g^{\text{eff}}(a) a \sqrt{\pi a}}{2 K_c} \right) = \frac{(1-\nu)}{4\mu} K_c \sqrt{\pi a} \left(\frac{a_3}{a} \right)^{3/2} \sim \frac{1}{a}. \quad (19)$$

The half thickness is the largest at the beginning of the growth and then steadily decreases proportional to a^{-1} . The ambient pressure, gradient, and half thickness, as well as some other parameter, are plotted in Figure 5.

[36] As before, the crack tip velocity is equated by assuming laminar flow as

$$\begin{aligned} v = 2 \frac{da}{dt} &= \frac{2}{3\eta} h^2 (g - g^{\text{eff}}) = \frac{(1-\nu)^2}{96\eta\mu^2} K_c^2 \pi a \left(\frac{a_3}{a} \right)^3 (g - g^{\text{eff}}) \\ &= \frac{(1-\nu)^2}{96\eta\mu^2} K_c^2 \pi a \left(\frac{a_3}{a} \right)^3 \left[g - \frac{2K_c}{a\sqrt{\pi a}} \left(1 - \left(\frac{a_3}{a} \right)^{3/2} \right) \right]. \end{aligned} \quad (20)$$

Equation (20) is related to the fixed coordinate system and is used to derive, upon integration, the theoretical relationship for $a(t)$. The crack velocity as a function of crack half-length a is plotted in Figure 6.

[37] The ratio of velocities at the beginning and end of phase 3 is

$$\frac{v}{v_3} = \frac{a_3^2}{a^2} \left(1 - \frac{g^{\text{eff}}(a)}{g} \right), \quad \text{and} \quad \frac{v_4}{v_3} = 2^{-4/3} \left(1 - \frac{P_0(a_3)}{2a_3 g} \right). \quad (21)$$

The ratio v_4/v_3 depends only on initial conditions and g . The end velocity v_4 is zero if $P_0(a_3) = 2a_3 g$. The ratio v_4/v_3 gives an independent method to estimate the gradient g and thus the pore pressure or tectonic stress gradients in the formation.

[38] In order to retrieve $a(t)$ and $v(t)$ as a function of time the differential equation has to be integrated numerically (Figure 6). The normalized presentation of the time-dependent half-length is clearly influenced from ga_3 , and vice versa, g and possibly K_c can be retrieved by modeling the time-dependent length of the fracture during the post-injection phase with unidirectional growth.

[39] The opening shape of the fracture controls the stress changes in the surrounding rock. Inserting (13) into (12) leads to

$$\begin{aligned} \Delta u(x', a) &= \frac{(1-\nu)}{\mu} \left(2 \frac{K_c}{\sqrt{\pi a}} + g^{\text{eff}}(a) [x' - a] \right) \sqrt{a^2 - (x')^2} \\ &= 2 \frac{(1-\nu)}{\mu} \frac{K_c}{\sqrt{\pi a}} \left\{ 1 + \left[\frac{x' - a}{a} \right] \left(1 - \left(\frac{a_3}{a} \right)^{3/2} \right) \right\} \\ &\quad \cdot \sqrt{a^2 - (x')^2}, \end{aligned} \quad (22)$$

for $a_3 \leq a \leq 2^{2/3}a_3$. For $a = a_3$ the fracture has an elliptical shape, and for $a = 2^{2/3}a_3$ the fracture opening and its first derivative are zero at the tip of the shorter wing at $x' = -a$ or at $x = 0$.

[40] The position of maximal opening, x'_{max} , moves in direction of unidirectional growth and is given by

$$\begin{aligned} x'_{\text{max}} &= \frac{-P_0(a) \pm \sqrt{(P_0(a))^2 + \frac{1}{2}(2ag^{\text{eff}}(a))^2}}{2g^{\text{eff}}(a)} \\ &= a \frac{-\left(\frac{a_3}{a}\right)^{3/2} \pm \sqrt{9\left(\frac{a_3}{a}\right)^3 - 16\left(\frac{a_3}{a}\right)^{3/2} + 8}}{4\left(1 - \left(\frac{a_3}{a}\right)^{3/2}\right)}. \end{aligned} \quad (23)$$

[41] A plot of the opening shape of the fracture at different times (fracture length) is given in Figure 7 (left; $g = 0$ for Figures 7a and 7b; $g > 0$ for Figure 7c). The position of the

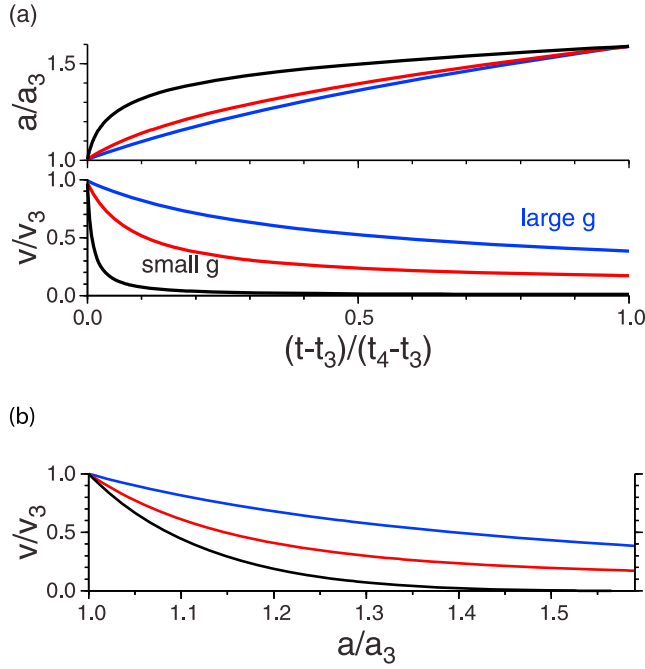


Figure 6. Fracture tip velocity v is plotted as function of (a) normalized time and (b) normalized length for different values of $ga_3 = 10$ MPa, 0.5 MPa, and 0.282 MPa. The normalized time-dependent half-length is given in Figure 6a (top). Note that the smallest gradient is $g = 1.028P_0(a_3)/(2a_3)$. See Figure 5 for further reference.

maximal opening should correlate with the back front of ceasing seismicity since the stress magnitude decreases in the region that has been passed by the thickest part of the fracture. It is interesting that x'_{\max} does not depend on dynamic parameters but only on the geometry of the problem. The maximal opening is at position $x' = 0$ when the unidirectional propagation begins ($x = a_3$ in the absolute system) and at relative position $x' = a(t_4)/2 = a_4/2$ at time t_4 ($x = 3a_4/2$ in the absolute system). In absolute coordinates the position of the back front (x_{\max}) and front (x_+) of the seismicity is expected to be roughly at

$$x_{\max}(t) = x'_{\max}(t) + a(t) \quad \text{and} \quad x_+ = 2a(t), \quad (24)$$

respectively.

2.5. Wholesale Fracture Movement: Postinjection Phase 4

[42] Depending on the size of the fracture at time $t = t_4$, or the remaining overpressure, the fracture may experience a slow wholesale migration in direction of driving stress gradient for $t > t_4$. This process has been discussed in several

papers [e.g., Weertman, 1971b; Dahm, 2000b, 2000a] and is not discussed here.

2.6. Stress Changes and Seismicity Pattern

[43] The solutions can be used to predict the stress changes in the medium. We adapt a boundary element method [Crouch and Starfield, 1983] to calculate the fracture-induced stress in a homogeneous infinite medium. The fracture is represented by elements of constant length and dislocation. Theoretical Green functions are used to calculate the influence from each boundary source to any point Q in the full or half-space. The superposition of Green functions gives strain and stress at Q . We calculate at Q the principal stress magnitudes σ_1 and σ_2 and from this the maximal normal (σ_n), shear (σ_s), and Coulomb stress (σ_c) for a friction coefficient of $f = 0.8$. Pore pressure changes have not been considered. A background stress may be added to the induced stress if significant tectonic shear stress is postulated, and this would possibly change the pattern of Coulomb stress. However, often the induced shear stress close to the fracture is larger than the tectonic shear stress. It is thus omitted in our application here.

[44] According to Coulomb's failure criterion the triggering of microearthquakes is promoted within volumes where σ_c is increasing with time [e.g., Becker et al., 2010]; that is, where the Coulomb stress rate $\Delta\sigma_c/\Delta t$, or $\Delta\sigma_c/\Delta a$, is positive. The Coulomb stress rate has been estimated on favorably oriented fault planes. Figure 7 shows the evolution of the opening shape and the associated patterns of positive Coulomb stress rate. The fracture is assumed to grow continuously, and three snapshots for different fracture lengths, indicated in the top left corner of each panel, are simulated for each of phases 1 to 3. Figure 7 (left) shows the evolution of the opening shapes during the continuous growth. Note that the scale of vertical axes changes between phases 1 and 3 and that the horizontal axes are scaled to their maxima during each phase. Figure 7 (right) shows the normalized Coulomb stress change per unit length increase of the fracture. Phases 1 and 2 have been simulated for $g = 0$, while in phase 3 we assume $g > 0$. For each of the three snapshots in the phases 1 to 3, the induced earthquakes are expected in the red regions with positive Coulomb stress rate. During injection phase 1 the seismicity occurs over the whole length of the fracture and the Coulomb stress rate is large. This justifies the common approach to estimate the orientation and length of the hydrofracture from the cloud of induced seismicity. However, a closer look indicates that the actual length of the fracture is slightly smaller than the extent of the expected seismicity cloud.

[45] During postinjection phase 2 the fluid and growth reorganize, and the fracture is in a stage of self-expansion under constant volume. The Coulomb stress rate decreases with expansion of the fracture. It is noteworthy that the

Figure 7. (left) Normalized fracture opening in phases (a) 1, (b) 2, and (c) 3 for three lengths of a , at the beginning (black), in the middle (red), and at the end of the period (blue) ($g = 0$ for Figures 7a and 7b, $g > 0$ for Figure 7c). The opening shape at the beginning of phase 3 is elliptical (black line in Figure 7c). (right) Normalized Coulomb stress change per incremental length increase of $0.01a$ is plotted in a x - y plane for the three different stages. The frictional coefficient was 0.8. The contoured stress change $\Delta\sigma_c$ is normalized to approximately the same relative scale. The fracture was discretized by 100 boundary elements of constant dislocation. The grey inverted triangle indicates the position of maximal opening.

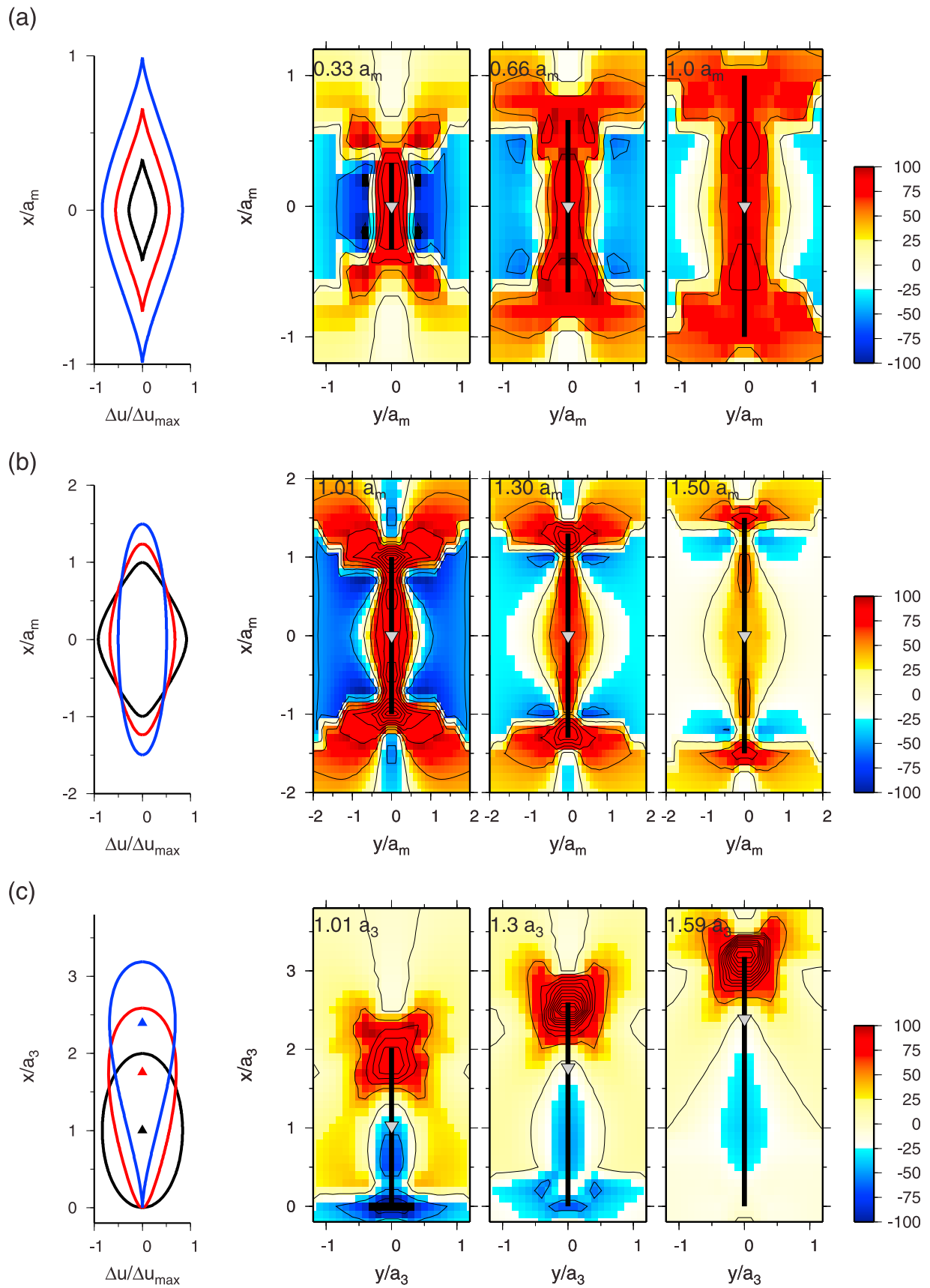


Figure 7

strongest decrease in Coulomb stress rate is in the middle of the fracture. If a smaller coefficient of friction is used, the middle of the fracture may even experience a negative Coulomb stress rate; that is, earthquakes are rarely induced in the middle part. This may explain observations of seismic back fronts during the postinjection phase.

[46] Most interesting in our case is the postinjection phase 3, where unidirectional fracture growth is observed. At the end of phase 2 and the beginning of phase 3 the potential of inducing seismicity decreases for a short time period; that is, we expect fewer earthquakes during this phase. We will see below that this is observed in real data examples. Interestingly, the red regions move unidirectional in the same direction as the tip of the growing longer wing, and a sharp transition to a region with no expected earthquakes develops behind the propagating tip. The transition zone between earthquakes and no earthquakes is approximately at the position of the maximal opening of the fracture. Since the maximal opening position at the beginning of phase 3 is in the middle of the fracture, the back front of seismicity has its origin in the middle of the fracture at time t_3 . The modeling thus confirms the hypothesis that a unidirectional propagation of a seismic cloud during the postinjection phase is associated with the unidirectional propagation of the hydrofracture.

[47] Figure 7 contains more information than the prediction of fore and back front of induced seismicity. The rate of seismicity, as well as the strength of events, may be quantitatively related to the rate of Coulomb stress during fracture growth and possibly used to derive a better kinematic fracture model in applications.

3. Application to Hydrofracturing Experiment and Discussions

[48] In 2005 a well in the Sawyer Canyon Sands gas field of west Texas was completed by hydraulic fracturing over six depth intervals. Such completions are routinely done in the field to stimulate production from the low-permeability sandstones. Microseismic monitoring was performed for all six hydraulic fracture stimulations [e.g., Fischer *et al.*, 2008]. The well was nearly vertical, and the six stimulation stages were conducted over isolated intervals ranging from 10 to 34 m at depths between 1518 and 1858 m. In 2005, six hydraulic fracturing experiments in a low-permeability gas field in the Canyon sandstone, west Texas, have been performed in order to stimulate the field and increase the productivity of the producing sands [e.g., Fischer *et al.*, 2008]. The nearly vertical borehole at a depth between 1518 and 1858 m was sealed off in intervals between 10 and 34 m. The casing was perforated in these intervals, and each stimulation lasted about 30 min at a wellhead pressure between 25 and 30 MPa. Assuming a hydrostatic gradient in the well, the downhole overpressure was possibly between 3 and 8 MPa. However, since the viscosity of the injection brine was increased by adding a low concentration of polymer and CO₂ to reduce fluid leak off, the downhole overpressure (net pressure) was possibly smaller. In each stage, more than 100 m³ of fracturing fluid and about 20 m³ of sand were injected into the reservoir formation.

[49] The seismic monitoring was conducted with a vertical array of eight three-component geophones installed at depth between 1604 and 1817 m (30 m spacing) within a second

borehole about 250 m from the injection borehole. Location errors are about ± 20 m. The experiments and localization technique are further described by Eisner *et al.* [2006] and Fischer *et al.* [2008].

[50] All stimulation experiments induced numerous micro-earthquakes. A characteristic feature was the asymmetric bidirectional growth of the seismic cloud during the injection and the unidirectional growth during the postinjection phase. The asymmetric growth during injection has been interpreted by Fischer *et al.* [2009] by means of driving stress gradients. Here, we concentrate on the unidirectional growth of the seismic cloud during the postinjection phase and the behavior of the fore and back front of seismicity.

[51] Figures 8 and 9 show the time-dependent position of induced earthquakes projected along the strike direction of the hydrofracture. The distance-time plots can be used to estimate a parameterized fore and back front of the seismicity by means of a maximum likelihood method [Fischer *et al.*, 2008]. This is justified if the time-dependent downhole pressure has not been measured during the injection phase 1. Comparing the relative lengths of the short and long wings is sufficient to estimate the gradient g [Fischer *et al.*, 2009]. In this paper we demonstrate that all three phases, 1–3, can be modeled with a consistent set of parameters and a single gradient g . For this, it is sufficient to keep the downhole overpressure (net pressure at $x = 0$) constant during phase 1.

[52] The front of seismicity is assumed to be slightly ahead of the tip of the fracture. The back front of seismicity is defined by the position of x_{\max} . The duration of the injection has been measured and is indicated in Figures 8 and 9. Phase 3 begins at time t_3 and ends at time t_4 . Other times and lengths a_m , a_3 and a_4 have been inferred from the geometry of the seismic cloud. Using these constraints, both the front and back front of seismicity are well fitted in stage 3 (Figure 8) and stage 2 (Figure 9) of the hydrofracturing experiments. The parameters used are given in the captions for Figures 8 and 9.

[53] Figures 8 and 9 give an overview and show the seismicity of the postinjection phase in a zoomed section. The length increase of the longer wing, as well as the position of x_{\max} , are independent of fluid viscosity, net pressure, fracture toughness, elastic constants, or driving stress gradient. They are independent on external parameters and cannot be tuned to fit the data. In both cases, the model predicts very well the geometry of the front and back front during phase 3, which we interpret as a very strong support of the model presented.

[54] It can be recognized, especially in Figure 9, that the number of events decreases shortly before phase 3 begins at time t_3 . This behavior can possibly be associated with the reshaping of the fracture opening before unidirectional growth begins and was indicated by the modeling of Coulomb stress changes (e.g., Figure 7).

[55] The origin of the seismic back front is in the middle of the fracture at time t_3 , i.e., at position $(x + a_3)/a_3$ in Figures 8 and 9 (bottom). This was also predicted by the modeling of Coulomb stress changes (Figure 7). The curvature of the front and back front during the postinjection phase 3 depends only on the driving stress gradient g and K_c (or $P_0(a_3)$, see equations (21) and (24)) and are well explained in both stages with a common driving stress gradient

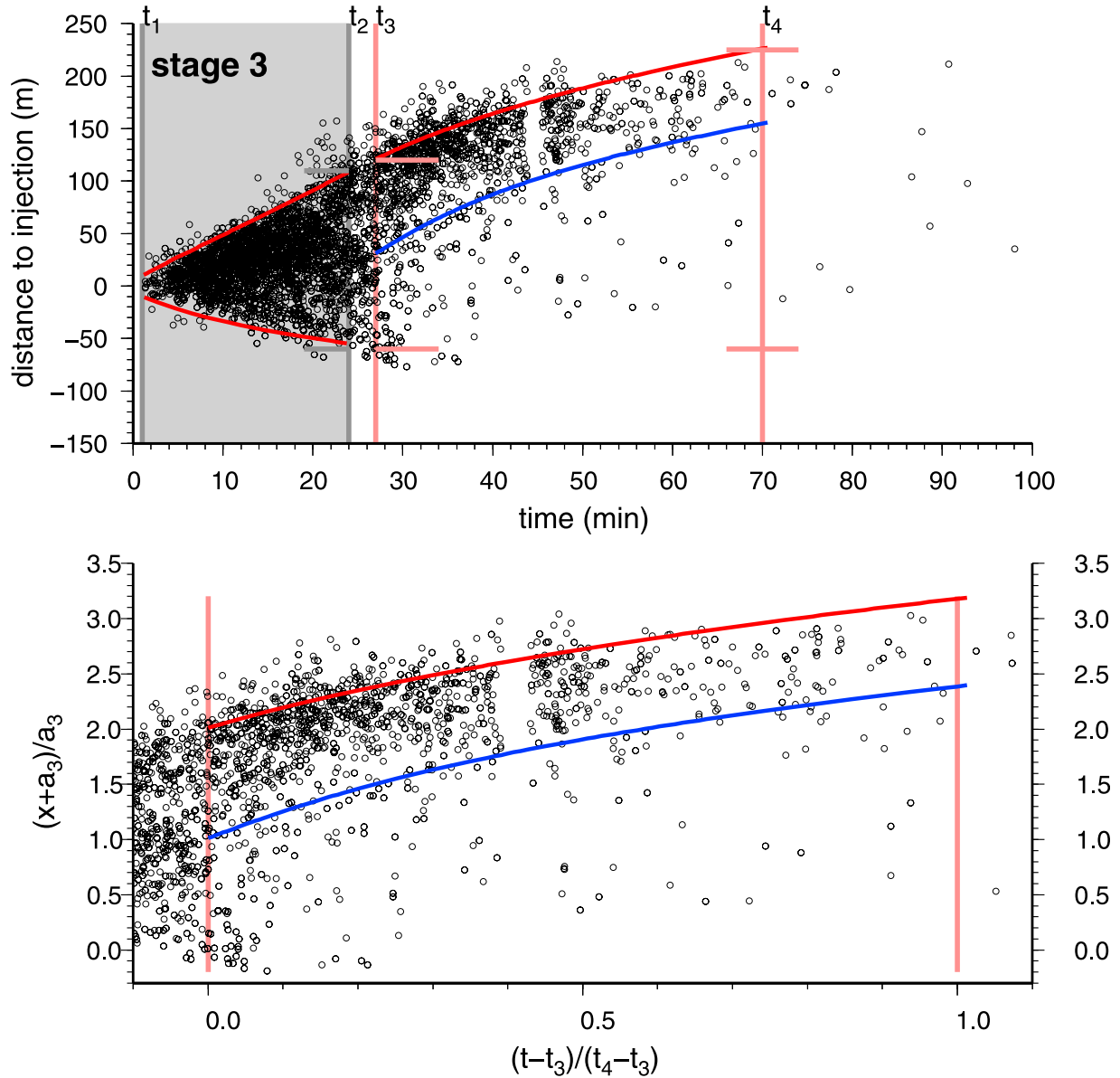


Figure 8. Distance versus time plot of the seismic cloud of injection experiment stage 3. The theoretical front and back front as derived by formulas (7) and (20) are plotted as red and blue lines, respectively. The injection period lasted from time $t_1 = 1$ min to $t_2 = 24$ min (grey area). The red ticks indicate the lengths of short and long wings from which the half-lengths $a_3 = 90$ m and $a_4 = 142.5$ m were measured. Other geometrical parameters have been estimated from the pattern of the seismicity and are indicated ($t_3 = 27$ min, $t_4 = 70$ min, $a_m = 85$ m). The dynamic parameters to obtain the fit were $P_0 \approx 0.7$ MPa, $g = 10$ MPa km $^{-1}$, $K_c \approx 1$ MPa m $^{1/2}$, $q_0 = 0.6 \times 10^{-2}$ m 2 s $^{-1}$, $\mu = 10$ GPa, $\nu = 0.25$, $\eta = 150$ Pa s.

of g larger than 0.8 MPa km $^{-1}$. In order to fit the seismicity front during the injection phase 1 the ratio g/P_0 has to be chosen at 10 and 14 km $^{-1}$ for stages 2 and 3, respectively. Assuming a net injection pressure of $P_0 = 1$ MPa for stage 2, the net pressure gradient is estimated at 10 MPa km $^{-1}$. This is similar to the value derived by Fischer *et al.* [2009]. A smaller net pressure would lead to a smaller gradient, and vice versa, a larger net pressure to larger gradient. However, the limiting value for g is 0.8 MPa km $^{-1}$, and we find a small difference between stages 2 and 3. For instance, assuming $g = 10$ MPa km $^{-1}$, the net pressure for stage 2 is

$P_0 \approx 1$ MPa and the influx volume rate is $q_0 \approx 0.3 \times 10^{-2}$ m 2 s $^{-1}$. For stage 3 the associated values are $P_0 \approx 0.7$ MPa and $q_0 \approx 0.6 \times 10^{-2}$ m 2 s $^{-1}$. The net injection pressure during stage 2 is predicted larger than the one for stage 3, and the influx volume rate just the opposite, smaller for stage 2 and larger for stage 3. This may be explained because the injection phase at stage 3 lasted about 24 min and $a_3(t_3)$ was about 90 m, while for stage 2 it lasted only 19.5 min and $a_3(t_3)$ was about 61 m. A longer fracture can be driven with a smaller overpressure compared to a shorter one, supporting the indication that $P_0(t_3)$ was larger for the shorter fracture.

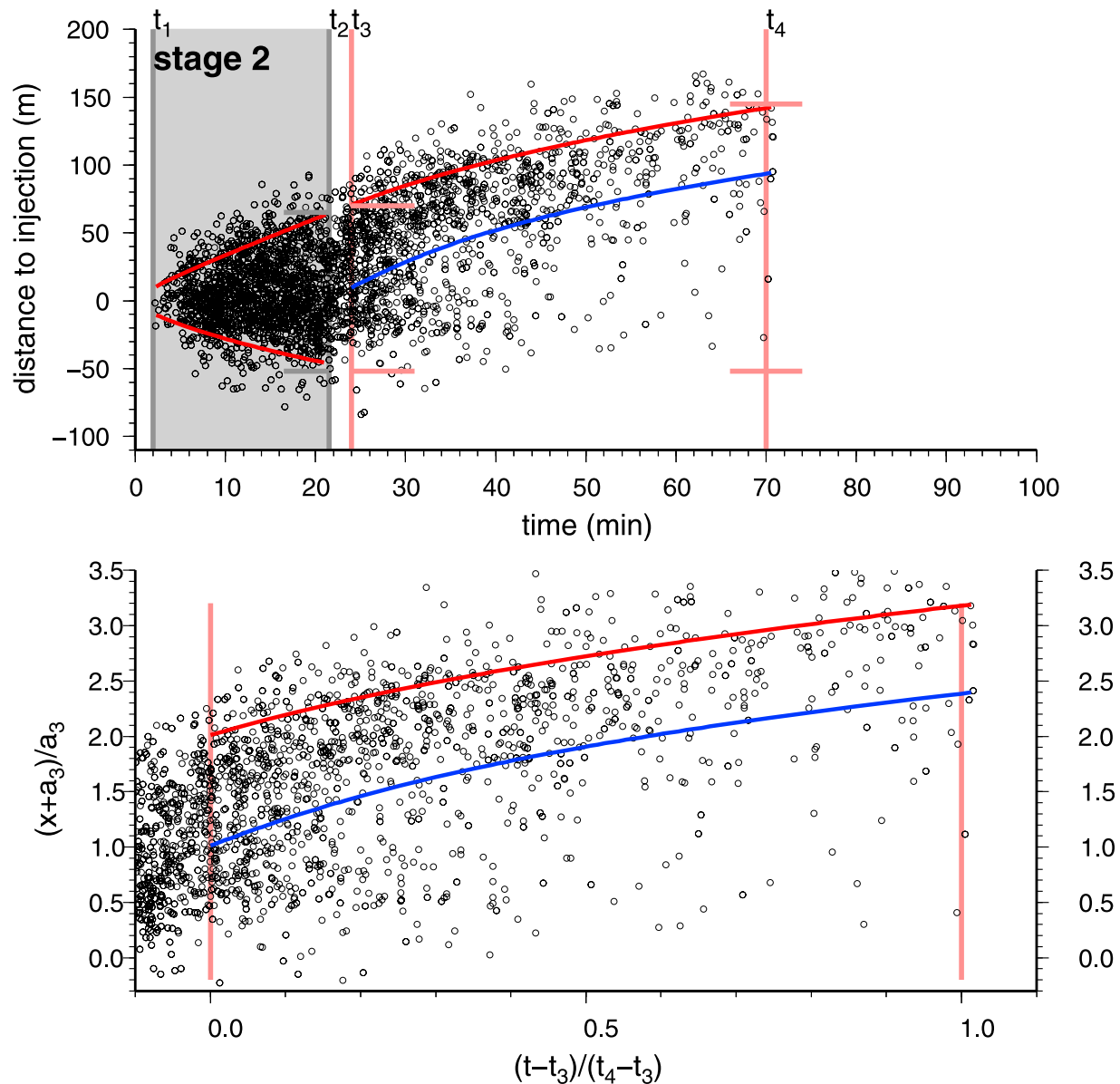


Figure 9. Distance versus time plot of the seismic cloud of injection experiment stage 2 lasting from $t_1 = 2$ min to $t_2 = 21.5$ min (grey area). Geometrical parameters were $t_3 = 24$ min, $t_4 = 70$ min, $a_m = 58.5$ m, $a_3 = 61$ m, $a_4 = 98.5$ m, and dynamic parameters to obtain the fit were $P_0 \approx 1$ MPa, $g = 10$ MPa km⁻¹, $K_c \approx 1$ MPa m^{1/2}, $q_0 = 0.3 \times 10^{-2}$ m² s⁻¹, $\mu = 10$ GPa, $\nu = 0.25$, $\eta = 150$ Pa s. See Figure 8 for further explanations.

Another possibility might be that the net pressure at the tip had more time to be reduced if the injection lasted longer.

[56] Absolute velocities depend on many more parameters than the net pressure or the stress gradients. The parameters chosen to model the injection phases 1 and 2 in Figures 8 and 9 are in a realistic range but are mutually dependent and not well resolved. Other combinations of parameters may possibly behave equally well. Additionally, the downhole pressure and flow rate was possibly not stationary during injection. The main goal here is to demonstrate that absolute values of nonlinear growth velocities, seismicity, and fracture length can be modeled by means of realistic parameters. We need relatively small values of net pressure $P_{\text{net}}(x = 0)$ and fracture toughness K_c to consistently model the complete

sequence from phase 1 to 3. K_c is only about 1 MPa m^{1/2}, which is much smaller than values estimated from the shape of solidified magmatic dikes in hard rock. A possible reason might be that the fracture was driven in a porous sandstone of a gas field, which can be assumed to be mechanically much weaker than hard crystalline rock. Another reason might be that preexisting fractures existed. The low values of ambient net pressure might indicate that the pressure loss is significant from the injection point down to the fracture itself. Unfortunately, no downhole pressures have been measured during the experiments.

[57] It has often been argued that the tip pressure and a fracture criterion can be neglected to understand the growth of hydrofractures. Our model, on the other hand, needs a

fracture criterion and a nonzero fracture toughness to explain postinjection growth. While the viscous pressure drop may control the overpressure along the length of the fracture and thus the shape of the fracture and the average opening, the tip pressure and the fracture toughness will control the growth and stopping of the fracture. Even if the viscous pressure drop was huge compared to the remaining driving pressure at the tip, it is the small remaining driving pressure that decides in our model whether the fracture continues to grow or not.

4. Conclusion

[58] The presented model is the first hydrofracturing model that considers stress gradients and quantifies the effect of postinjection bidirectional and unidirectional growth. We derive analytical equations to predict the fracture length and growth velocity and their interrelation to stress, downhole and formation pore pressure, or parameters of the fluid. The model is simplifying and so far does not account for storage, fluid leak off, non-Newtonian fluids, or 3-D geometry because we mainly aim to clarify the principal physical effects. However, we believe that the 2-D model can already be used to make first estimates on the stress gradients from field experiments. This belief is supported by the good fit between model predictions and observations in a gas field in Texas. The estimated lateral stress gradient (e.g., pore pressure gradient) is in the range of 10 MPa km⁻¹ (assuming a net pressure of $P_0 \approx 1$ MPa) and on the order of the vertical hydrostatic gradient. The proposed model has further been used to estimate time-dependent Coulomb stress changes and thus provides a direct theoretical link between rock emplacement and Coulomb stress-induced seismicity during hydrofracturing.

Appendix A: Static Fracture Solutions Under Stress Gradients

A1. Driving Stress With Constant Gradient

[59] The effects of gradients in the regional stress, or gradients in the internal pressure of the fracture, have been first analyzed by, e.g., *Weertman* [1971a] and *Pollard and Mueller* [1976]. We assume that the crack center is at $x = 0$ and the crack half-length is a . The effective driving stress acting on the crack wall is defined by

$$P(x) = P_0 + gx. \quad (A1)$$

where g is here for simpler notation the gradient of driving stress.

[60] The opening displacement $\Delta u_y = \Delta u$ of the crack wall is given by (Figure A1)

$$\Delta u = \frac{(1-\nu)}{\mu} (2P_0 + gx) \sqrt{a^2 - x^2}, \quad (A2)$$

where $-a \leq x \leq a$. $P_0 \geq ag/2$; otherwise, the fracture would close at tip of the shorter wing. The opening shape of the fracture may, in general, vary from elliptical to teardrop shape.

[61] The cross-sectional area A of the fracture, i.e., the volume per unit depth, is

$$A = \frac{(1-\nu)}{\mu} \pi a^2 P_0. \quad (A3)$$

Note that the cross-sectional area of a 3-D fluid-filled fracture under stress gradients equals the one given here [e.g., *Dahm*, 2000b]. From A the average half thickness of the fracture can be equated by

$$h = \frac{A}{4a} = \frac{(1-\nu)}{4\mu} \pi a P_0. \quad (A4)$$

It is interesting that the cross-sectional area A , or the average half thickness h , are independent of the gradient.

[62] The slope of the opening is then

$$\frac{d\Delta u}{dx} = \frac{(1-\nu)}{\mu} \left[-\frac{2P_0x + gx^2}{\sqrt{a^2 - x^2}} + g\sqrt{a^2 - x^2} \right], \quad (A5)$$

and has its maximum at

$$x_{\max} = \frac{-P_0 \pm \sqrt{P_0^2 + \frac{1}{2}(2ag)^2}}{2g}. \quad (A6)$$

[63] The stress intensity at the tips of a fracture is, in general [e.g., *Hahn*, 1976; *Pollard and Segall*, 1987],

$$K^\pm = \frac{1}{\sqrt{\pi a}} \int_{-a}^a P_0(s) \sqrt{\frac{a \pm s}{a \mp s}} ds. \quad (A7)$$

[64] For linearly varying driving stress we find [e.g., *Weertman*, 1971a; *Pollard*, 1976]

$$K^\pm = \sqrt{\pi a} \left(P_0 \pm \frac{g}{2} a \right). \quad (A8)$$

[65] A teardrop opening shape, a so-called Weertman fracture, is retrieved when stress intensity factor at the tip of the shorter wing is $K^-(a) = 0$. Then, the fracture closes at $x = -a$ under a horizontal slope, $d\Delta u/dx|_{x=-a} = 0$. The opening shape of the teardrop fracture may be simplified to

$$\Delta u = -\frac{(1-\nu)}{\mu} g(a+x) \sqrt{a^2 - x^2}. \quad (A9)$$

A2. Symmetric Loading With Gradients

[66] Symmetric loading with gradients has been analyzed for geological problems by *Weertman* [1971a] and *Pollard* [1976]. The effective driving stress acting on the crack wall is now defined by

$$P(x) = P_0 + \begin{cases} g_1 x & \text{for } x \leq 0 \\ g_2 x & \text{for } x \geq 0 \end{cases}, \quad (A10)$$

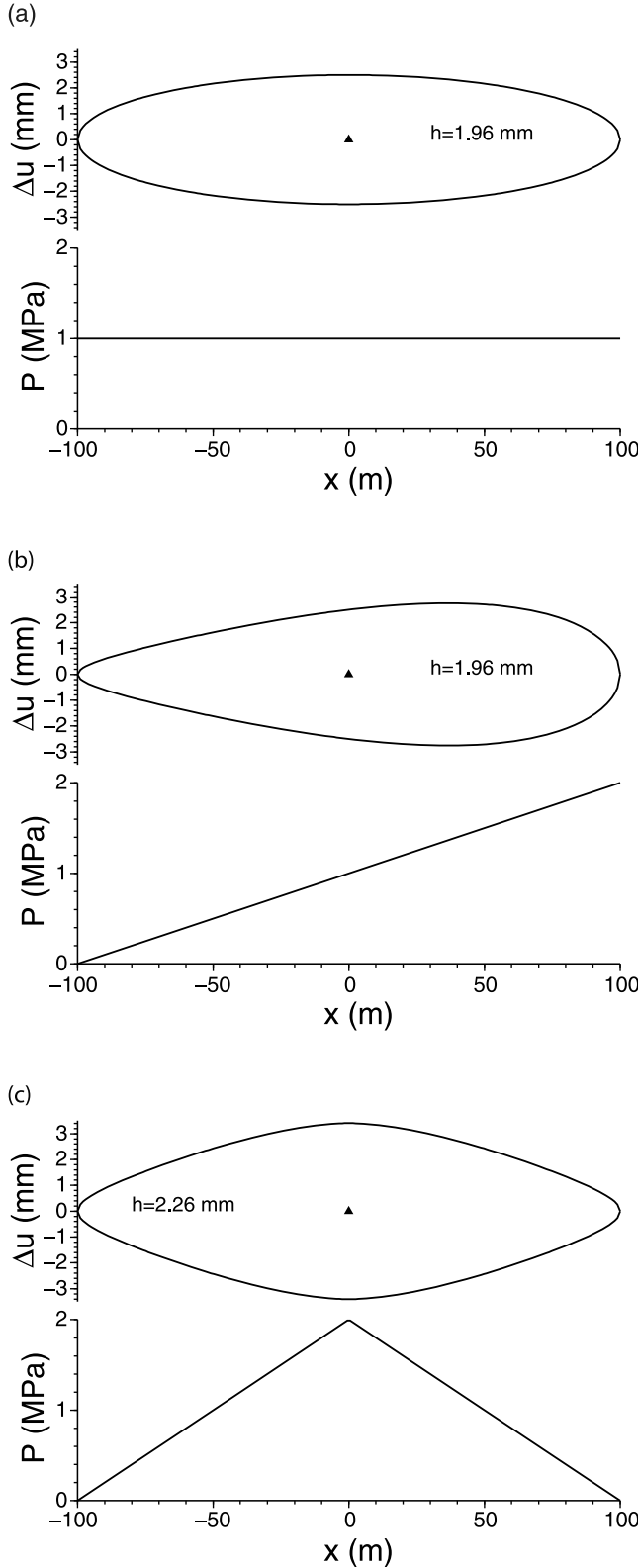


Figure A1. Opening shape of fractures under different types of pressure loading, i.e., (top) constant overpressure, (middle) constant pressure gradient, and (bottom) symmetric loading with gradients.

where $g = g_1 = -g_2$ and $g \geq 0$ is assumed. The opening dislocation $\Delta u_y = \Delta u$ of the crack wall is [e.g., *Weertman, 1971a; Pollard, 1976*] (Figure A1)

$$\Delta u = \frac{(1-\nu)}{\mu} \cdot \left\{ \left(2P_0 - \frac{2}{\pi}ga \right) \sqrt{a^2 - x^2} - \frac{2}{\pi}gx^2 \ln \left| \frac{x}{a - \sqrt{a^2 - x^2}} \right| \right\}, \quad (\text{A11})$$

where $-a \leq x \leq a$.

[67] The average half thickness of the crack is calculated by integrating (A11), leading to

$$h = \frac{1}{4a} 2 \int_0^a \Delta u dx = \dots = \frac{(1-\nu)}{4\mu} \pi a P_0 \left(1 - \frac{4}{3\pi} \frac{ga}{P_0} \right). \quad (\text{A12})$$

[68] The average opening of the crack decreases with increasing gradient g if P_0 at the midpoint $x = 0$ is held constant. If the ambient pressure at point $x = 4a/3\pi$ would be held constant, the opening would not change for varying gradients.

[69] The stress intensity at the tip of the longer and shorter wing of the fracture can be calculated by (A7) and is [see *Pollard, 1976*, formula (6)]

$$K^\pm = \sqrt{\pi a} \left(P_0 - \frac{2}{\pi}ga \right) = \sqrt{\pi a} \begin{cases} P_0 - \frac{2}{\pi}g_1a & \text{for } x \leq 0 \\ P_0 + \frac{2}{\pi}g_2a & \text{for } x \geq 0 \end{cases}. \quad (\text{A13})$$

A3. Asymmetric Loading With Gradients

[70] The most general profile of the driving stress is (Figure A2)

$$P(x) = \begin{cases} P_2 + g_2x = P_0 + g_2a' + g_2x & \text{for } -a' \leq x \leq a \\ P_1 + g_1x = P_0 + g_1a' + g_1x & \text{for } -a \leq x \leq -a' \end{cases}$$

$$\text{with } a' = \frac{a_2 - a_1}{2}$$

The injection point is asymmetric at point $-a'$.

[71] We equate the stress intensity at the tip of the longer wing by solving (A7),

$$\begin{aligned} \sqrt{\pi a} K_2 &= \int_{-a}^{-a'} [(P_0 + g_1a') + g_1s] \sqrt{\frac{a+s}{a-s}} ds \\ &+ \int_{-a'}^a [(P_0 + g_2a') + g_2s] \sqrt{\frac{a+s}{a-s}} ds. \end{aligned}$$

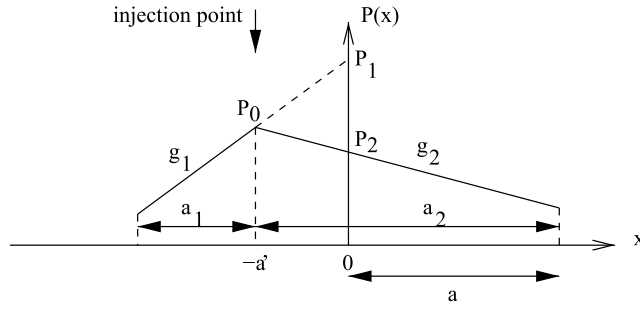


Figure A2. Sketch of pressure profile of an injection crack with two gradients of driving stress, g_1 and g_2 , and two lengths, a_1 and a_2 . The half-length of the crack is $a = (a_1 + a_2)/2$, and we assume $a_2 \geq a_1$ and $g_1 \geq g_2$. The injection point is asymmetric at point $-a'$. The injection pressure is P_0 . The stress intensity at the tip of the shorter wing is K_1 ; the one at the tip of the longer wing is K_2 .

[72] Using the integral formula (B2), we find

$$\begin{aligned} \sqrt{\pi a} K_2 &= \pi a P_0 + \pi a g_1 \left(\frac{a}{2} + a' \right) + (g_2 - g_1) \frac{2a + a'}{2} \\ &\quad \cdot \sqrt{(a + a')(a - a')} + (g_2 - g_1) a(a + 2a') \\ &\quad \cdot \sin^{-1} \left(\sqrt{\frac{a + a'}{2a}} \right) \\ &= \pi a P_0 + g_2 \left[\frac{2a + a'}{2} \sqrt{(a + a')(a - a')} \right. \\ &\quad \left. + a(a + 2a') \sin^{-1} \left(\sqrt{\frac{a + a'}{2a}} \right) \right] \\ &\quad - g_1 \left[\frac{2a + a'}{2} \sqrt{(a + a')(a - a')} + a(a + 2a') \right. \\ &\quad \left. \cdot \left\{ \sin^{-1} \left(\sqrt{\frac{a + a'}{2a}} \right) - \frac{\pi}{2} \right\} \right]. \end{aligned} \quad (\text{A14})$$

[73] The stress intensity factor at the tip of the shorter wing, K_1 , is equated from (A14) by interchanging the index of g_i and changing the sign of g_i and a' so that

$$\begin{aligned} \sqrt{\pi a} K_1 &= \pi a P_0 - g_1 \left[\frac{2a - a'}{2} \sqrt{(a + a')(a - a')} \right. \\ &\quad \left. + a(a - 2a') \sin^{-1} \left(\sqrt{\frac{a - a'}{2a}} \right) \right] \\ &\quad + g_2 \left[\frac{2a - a'}{2} \sqrt{(a + a')(a - a')} + a(a - 2a') \right. \\ &\quad \left. \cdot \left\{ \sin^{-1} \left(\sqrt{\frac{a - a'}{2a}} \right) - \frac{\pi}{2} \right\} \right]. \end{aligned} \quad (\text{A15})$$

[74] If $a' = 0$ ($a_1 = a_2 = a$) and $g_1 = g_2$, the stress intensity is equal to the one in (A8). K_2 in (A14) is equal to K^- in (A8) if $g_2 < 0$ and $a' \rightarrow a$, i.e., if the injection point moves toward the tip of the shorter wing. Note that for comparing this case the internal pressure has to be equated to the same point, e.g., the midpoint of the fracture.

[75] In the case of symmetric loading with $a' = 0$ ($a_1 = a_2 = a$) and $g_1 = -g_2$, the stress intensity is equal to (A13). Equations (A14) and (A15) can be expressed in terms of a_1 and a_2 when replacing $a = (a_2 + a_1)/2$ and $a' = (a_2 - a_1)/2$.

[76] Figure A3 shows the stress intensity factor at the tip of the longer wing as a function of parameter a' , i.e., of the shift of the injection point in negative direction. Three different values of the pressure gradient, $ag_2/P_0 = 0, 0.25$ and 0.5 are shown. The stress intensity slightly decreases with increasing value of asymmetry a' and with increasing value of gradient g_2 . The correct values are compared to the approximations in (A13) and (A8). For a zero gradient, $g_2 = 0$, the two approximations give the exact values. If $g_2 < 0$, equation (A13) gives fairly good estimate as long as $a'/a < 0.4$.

Appendix B: Integral Formula

[77] The integral of one type is

$$I_1 = \int_{a_1}^{a_2} \sqrt{\frac{a+s}{a-s}} ds \quad \text{and} \quad I_2 = \int_{a_1}^{a_2} s \sqrt{\frac{a+s}{a-s}} ds. \quad (\text{B1})$$

[78] Substitution of $u = a - s$ ($s = a - u$, $ds/du = -1$, $a + s = a + a - u = 2a - u$) gives

$$I_1 = - \int_{a-a_1}^{a-a_2} \sqrt{\frac{2a-u}{u}} du$$

and

$$I_2 = - \int_{a-a_1}^{a-a_2} (a-u) \sqrt{\frac{2a-u}{u}} du = \int_{a-a_1}^{a-a_2} u \sqrt{\frac{2a-u}{u}} du + a I_1.$$

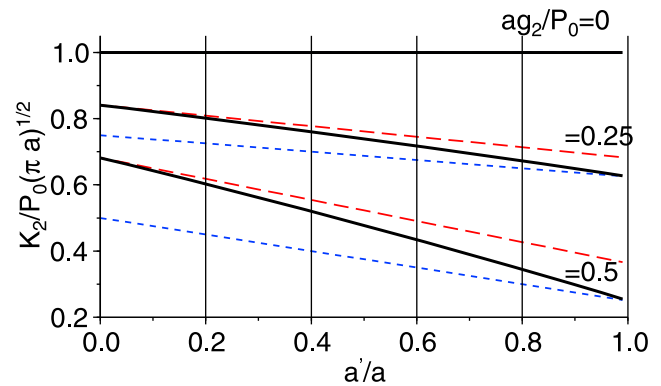


Figure A3. K_2 (black continuous line) is plotted as a function of a' for different parameters of the gradient g_2 . The K^+ approximated by (A13) (long dashed line, using $a = a_2$) and by (A8) (short dashed line) are plotted for comparison.

[79] Substitution of $v = \sqrt{u}$ ($u = v^2$, $du/dv = 2v$) leads to

$$I_1 = -2 \int_{\sqrt{a-a_1}}^{\sqrt{a-a_2}} \sqrt{2a-v^2} dv$$

$$I_2 = 2 \int_{\sqrt{a-a_1}}^{\sqrt{a-a_2}} v^2 \sqrt{2a-v^2} dv + aI_1.$$

[80] Using elementary root functions [e.g., *Bronstein and Semendjajew*, 1985] leads to

$$I_1 = - \left[v\sqrt{2a-v^2} + 2a \sin^{-1} \frac{v}{\sqrt{2a}} \right]_{\sqrt{a-a_1}}^{\sqrt{a-a_2}} \quad (B2)$$

$$I_2 = -2 \left[\frac{v}{4} (2a-v^2)^{3/2} \right]_{\sqrt{a-a_1}}^{\sqrt{a-a_2}} + \frac{a}{2} I_1. \quad (B3)$$

[81] When choosing $a_1 = -a$ and $a_2 = a$, the stress intensity at the tip of the longer wing is equated to $K^+ = \sqrt{\pi a}(P_0 + ga/2)$.

Notation

x, y, z, t Cartesian coordinates and time.

a position of fracture tip (>0).

a_s, a_l length of the short (s) and long (l) fracture wing during injection phase 1.

Δu opening (dislocation of fracture wall).

x_{\max} position of maximal opening.

h average half opening of the fracture.

A cross sectional area.

$v(x, t)$ average cross-sectional flow velocity.

$v(a)$ fracture tip velocity.

v_s, v_l short and long wing tip velocity during phase 1.

$q = 2hv$ influx volume rate.

σ_{yy} tectonic normal stress acting from outside on the fracture walls (compressive >0).

$\Delta\sigma_c$ Coulomb stress change.

P internal effective driving pressure (including flow).

P_p pore pressure in the porous formation, acting from outside on the fracture walls.

P_d internal downhole pressure (no flow).

α Biot's constant.

P_{net} internal net pressure (no flow), equal to $P_d - (\sigma_{yy} - \alpha P_p)$.

g gradient of P_{net} along x .

g^{eff} effective driving pressure gradient, equal to $g + g^v$.

g^v flow-induced pressure gradient.

K stress intensity factor at tips.

K_c fracture toughness.

η dynamic viscosity.

μ shear modulus.

ν Poisson's ratio.

viewers and the Associate Editor R. K. Nowack improved the clarity of the text and helped to clarify the plausible range of downhole net pressures during injection. The work of the third author was supported by Czech research project MSM0021620855.

References

- Becker, D., B. Cailleau, T. Dahm, and S. Shapiro (2010), Stress triggering and stress memory observed from acoustic emissions records in a salt mine, *Geophys. J. Int.*, **182**(2), 933–948, doi:10.1111/j.1365-246X.2010.04642.x.
- Bronstein, I., and K. Semendjajew (1985), *Taschenbuch der Mathematik*, 840 pp., Harri Deutsch, Frankfurt, Germany.
- Cornet, F., and P. Julien (1989), Stress determination from hydraulic test data and focal mechanisms of induced seismicity, *Int. J. Mech. Min. Sci. Geomech. Abstr.*, **26**, 235–248, doi:10.1016/0148-9062(89)91973-6.
- Cornet, F., and J. Yin (1995), Analysis of induced seismicity for stress field determination and pore pressure mapping, *Pure Appl. Geophys.*, **145**, 677–700, doi:10.1007/BF00879595.
- Crouch, S., and A. Starfield (1983), *Boundary Element Methods in Solid Mechanics*, 321 pp., Allen and Unwin, London.
- Dahm, T. (2000a), Numerical simulations of the propagation path and the arrest of fluid-filled fractures in the earth, *Geophys. J. Int.*, **141**, 623–638, doi:10.1046/j.1365-246x.2000.00102.x.
- Dahm, T. (2000b), On the shape and velocity of fluid-filled fractures in the earth, *Geophys. J. Int.*, **142**, 181–192, doi:10.1046/j.1365-246x.2000.00148.x.
- Dahm, T., G. Manthei, and J. Eisenblätter (1999), Automated moment tensor inversion to estimate source mechanisms of hydraulically induced micro-seismicity in salt rock, *Tectonophysics*, **306**, 1–17, doi:10.1016/S0040-1951(99)00041-4.
- Economides, M., and K. Nolte (2003), *Reservoir Stimulation*, John Wiley, Hoboken, N. J.
- Eisenblätter, J. (1988), Localisation of fracture planes during hydraulic fracturing experiments in a salt mine, in *Acoustic Emission*, pp. 291–303, Dtsch. Ges. für Metallkd., Oberursel, Germany.
- Eisner, L., T. Fischer, and J. Le Calvez (2006), Detection of repeated hydraulic fracturing (out-of-zone growth) by microseismic monitoring, *Leading Edge*, **25**, 548–554, doi:10.1190/1.2202655.
- Evans, K., H. Moriya, H. Niitsuma, R. Jones, W. Phillips, A. Genter, J. Sausse, R. Jung, and R. Baria (2005), Microseismicity and permeability enhancement of hydrogeologic structures during massive fluid injections into granite at 3 km depth at the Soultz HDR site, *Geophys. J. Int.*, **160**, 389–412, doi:10.1111/j.1365-246X.2004.02474.x.
- Fischer, T., L. Eisner, S. Shapiro, and J. LeCalvez (2008), Microseismic signatures of hydraulic fracture growth in sediment formations: Observations and modeling, *J. Geophys. Res.*, **113**, B02307, doi:10.1029/2007JB005070.
- Fischer, T., S. Hainzl, and T. Dahm (2009), The creation of an asymmetric hydraulic fracture as a result of driving stress gradients, *Geophys. J. Int.*, **179**, 634–639, doi:10.1111/j.1365-246X.2009.04316.x.
- Geertsma, J., and F. de Klerk (1969), A rapid method of predicting width and extent of hydraulic induced fractures, *JPT J. Pet. Technol.*, **21**, 1571–1581, doi:10.2118/2458-PA.
- Hahn, H. (1976), *Bruchmechanik*, 218 pp., B. G. Teubner, Stuttgart, Germany.
- House, L. (1987), Locating microearthquakes induced by hydraulic fracturing in crystalline rock, *Geophys. Res. Lett.*, **14**, 919–921, doi:10.1029/GL014i009p00919.
- Khrstianovich, S., Y. Zheltov, G. Barenblatt, and G. Maximovich (1959), Theoretical principles of hydraulic fracturing of oil strata, paper presented at Fifth World Petroleum Congress, New York.
- Manthei, G., J. Eisenblätter, and P. Kamlot (2003), Stress measurements in salt mines using a special hydraulic fracturing borehole tool, in *Proceedings of the International Symposium on Geotechnical Measurements and Modelling*, edited by O. Nataf, E. Fecker and E. Pimentel, pp. 355–360, A.A. Balkema, Karlsruhe, Germany.
- Moriya, H., T. Fujita, H. Niitsuma, H. Eisenblätter, and G. Manthei (2006), Analysis of fracture propagation behavior using hydraulically induced acoustic emissions in the Bernburg salt mine, Germany, *Int. J. Rock Mech. Min. Sci.*, **43**, 49–57, doi:10.1016/j.ijrmms.2005.04.003.
- Nordgren, R. (1972), Propagation of a vertical hydraulic fracture, *SPE J.*, **12**, 306–314.
- Nur, A., and J. D. Byerlee (1971), An exact effective stress law for elastic deformation in rock with fluids, *J. Geophys. Res.*, **76**, 6414–6419, doi:10.1029/JB076i026p06414.
- Oye, V., J. Chavarria, and P. Malin (2004), Determining SAFOD area microearthquake location solely with the pilot hole seismic array, *Geophys. Res. Lett.*, **31**, L12S10, doi:10.1029/2003GL019403.

[82] **Acknowledgments.** We acknowledge the discussion with colleagues during the development of the work. The comments of two re-

- Parotidis, M., S. Shapiro, and E. Rothert (2004), Back front of seismicity induced after termination of borehole fluid injection, *Geophys. Res. Lett.*, **31**, L02612, doi:10.1029/2003GL018987.
- Perkins, T., and L. Kern (1961), Width of hydraulic fractures, *JPT J. Pet. Technol.*, **13**(9), 937–949, doi:10.2118/89-PA.
- Pollard, D. (1976), On the form and stability of open hydraulic fractures in the Earth's crust, *Geophys. Res. Lett.*, **3**, 513–516, doi:10.1029/GL003i009p00513.
- Pollard, D. D., and R. C. Fletcher (2005), *Fundamentals of Structural Geology*, 497 pp., Cambridge Univ. Press, Cambridge, U. K.
- Pollard, D., and O. Mueller (1976), The effect of gradients in regional stress and magma pressure on the form of sheet intrusions in cross sections, *J. Geophys. Res.*, **81**, 975–984, doi:10.1029/JB081i005p00975.
- Pollard, D., and P. Segall (1987), Theoretical displacements and stresses near fractures in rock: With application to faults, joints, veins, dikes, and solution surfaces, in *Fracture Mechanics of Rock*, edited by B. K. Atkinson, pp. 277–347, Academic, San Diego, Calif.
- Rutledge, J., and W. Phillips (2003), Hydraulic stimulation of natural fractures as revealed by induced microearthquakes, Carthage Cotton Valley gas field, east Texas, *Geophysics*, **68**, 441–452, doi:10.1190/1.1567212.
- Rutledge, J., W. Phillips, and M. Mayerhofer (2004), Faulting induced by forced fluid injection and fluid flow forced by faulting: An interpretation of hydraulic-fracture microseismicity, Carthage Cotton Valley Gas Field, Texas, *Bull. Seismol. Soc. Am.*, **94**, 1817–1830, doi:10.1785/012003257.
- Shapiro, S. (2000), An inversion for fluid transport properties in three-dimensionally heterogeneous rocks using induced microseismicity, *Geophys. J. Int.*, **143**, 931–936, doi:10.1046/j.1365-246X.2000.00264.x.
- Shapiro, S. A., E. Huenges, and G. Borm (1997), Estimating the crust permeability from fluid-injection-induced seismic emission at the KTB site, *Geophys. J. Int.*, **131**, F15–F18, doi:10.1111/j.1365-246X.1997.tb01215.x.
- Shapiro, S. A., C. Dinske, and E. Rothert (2006), Hydraulic-fracturing controlled dynamics of microseismic clouds, *Geophys. Res. Lett.*, **33**, L14312, doi:10.1029/2006GL026365.
- Warpinski, N. (1985), Measurement of width and pressure in a propagating hydraulic fracture, *SPE J.*, **25**, 46–54.
- Weertman, J. (1971a), Theory of water-filled crevasses in glaciers applied to vertical magma transport beneath oceanic ridges, *J. Geophys. Res.*, **76**, 1171–1183, doi:10.1029/JB076i005p01171.
- Weertman, J. (1971b), Velocity at which liquid-filled cracks move in the Earth's crust or in glaciers, *J. Geophys. Res.*, **76**, 8544–8553, doi:10.1029/JB076i035p08544.
- Zoback, M. (2007), *Reservoir Geomechanics*, 499 pp., Cambridge Univ. Press, Cambridge, U. K., doi:10.1017/CBO9780511586477.

T. Dahm, Institut für Geophysik, Universität Hamburg, Bundesstr. 55, D-20146 Hamburg, Germany. (torsten.dahm@zmaw.de)

T. Fischer, Faculty of Science, Charles University in Prague, Albertov 6, Prague 2, 12843, Czech Republic. (fischer@natur.cuni.cz)

S. Hainzl, GFZ German Research Centre for Geosciences, Telegrafenberg, D-14473 Potsdam, Germany. (hainzl@gfz-potsdam.de)